Japanese Journal of Applied Physics

REGULAR PAPER

High-speed measurement of two-dimensional displacement of myocardium using element RF data of ultrasonic probe

To cite this article: Kaisei Hara *et al* 2023 *Jpn. J. Appl. Phys.* **62** SJ1040

Japanese Journal of Applied Physics **62**, SJ1040 (2023) **REGULAR PAPER**
https://doi.org/**10.35848/1347-4065/acc112**

High-speed measurement of two-dimensional displacement of myocardium using element RF data of ultrasonic probe

Kaisei Hara[1], Shohei Mori[2*], Mototaka Arakawa[1,2], and Hiroshi Kanai[1,2]

[1]*Graduate School of Biomedical Engineering, Tohoku University, Sendai, Miyagi 980-8579, Japan*
[2]*Graduate School of Engineering, Tohoku University, Sendai, Miyagi 980-8579, Japan*

[*]E-mail: mori@tohoku.ac.jp

Received November 15, 2022; revised February 16, 2023; accepted March 2, 2023; published online March 27, 2023

Improving the accuracy of heart wall motion measurement is essential to realise better cardiac function evaluation. This paper proposed a two-dimensional (2D) displacement estimation method with a high temporal resolution using the 2D complex cross-correlation of element RF signals of an ultrasonic probe between frames returned from the target scatterers. The application of the proposed method to the phantom displacement confirmed its principle. The estimated 2D displacement of the phantom was consistent with the set displacement. Subsequently, the method was applied to two healthy subjects to measure the 2D displacement of the interventricular septum during one cardiac cycle. Consequently, during systole and diastole, the movement of the myocardium was measured, and the results were validated.

1. Introduction

Echocardiography is useful for evaluating cardiac function owing to its repeatability, non-invasive diagnostic capability, and high temporal resolution. Consequently, various medical applications have been studied to evaluate cardiac function, including measuring heart wall strain rates[1–7] and propagation of response of the myocardium to contraction.[8–10] However, further enhancement of the accuracy of heart wall motion measurements is essential to realise better cardiac function evaluations.

The speckle tracking method was applied to measure the two-dimensional (2D) displacement between frames of the heart wall using the correlation window on the acquired B-mode image to track changes in the speckle position within the correlation window between consecutive frames.[11–17] By increasing the number of transmissions of the beam direction per frame, smaller sampling intervals in the lateral direction were achieved; however, the temporal resolution was reduced. In clinical practice, heart wall displacement has been measured with a temporal resolution in the slow range of 40–80 Hz for normal heart rates.[18–20]

However, in vivo measurements of the instantaneous displacement (velocity) along the ultrasonic beam of the heart wall revealed the existence of higher frequency components. Moreover, for these measurements, a higher frame rate (>400 Hz) is necessary to improve the accuracy of the velocity measurement.[10] Consequently, 2D displacement measurements require a similar high frame rate to maintain the accuracy.

To measure the 2D displacement of the heart wall with a high temporal resolution, a method for forming an arbitrary number of received beams per transmission of unfocused waves was proposed.[21–25] As unfocused wave transmission realises a spatially wider range of measurements, this technique significantly improves the temporal resolution and achieves a high density of scan lines in the lateral direction.[26,27] However, signals from other scatterers that move independently are also added and spatially averaged, which contaminates the amplitude of the receiving beam and affects the measurement of the 2D dimensional displacement.

The received time distribution of the RF waves of the probe elements scattered from the target changes according to the 2D displacement of the target. A method for measuring the 2D displacement without beam scanning was proposed by measuring the change in the received time distribution of the scattered waves.[28,29] However, these previous studies did not consider the actual distribution of the received time on probe elements. The received time distribution was approximated by using a linear function determined by the element position. These studies aimed to measure the 2D velocity vector of blood flow; however, the measurement of the 2D displacement of the heart wall was not fully considered.

The difference in the received time distribution is small because the 2D displacement of the heart wall between frames is smaller than that for blood flow. Thus, considering the actual distribution of the received time on probe elements is an effective strategy. Based on this principle, a method to estimate the 2D displacement by evaluating the root mean squared difference of the received time distribution from the geometrically calculated received time distribution was proposed.[30] However, the condition with multiple scatterers was not considered.

Thus, this study proposes a novel 2D displacement estimation method with a high temporal resolution. The 2D displacement was estimated using the 2D complex cross-correlation of RF signals of probe elements between frames, wherein RF signals were arranged by the received time distribution of scattered waves on the probe. The application of the proposed method to the phantom displacement confirmed its principle from the estimate of the 2D displacement of the phantom. Thereafter, the proposed method was applied to two healthy subjects and the 2D displacement of the interventricular septum (IVS) during one cardiac cycle was successfully measured.

2. Principles

2.1. 2D displacement estimation method using received time distribution of scattered waves on elements of ultrasonic probe

As illustrated in Fig. 1, consider the case wherein the target scatterer was set at $(x_s,\ z_s)$ at the nth frame and was displaced by $(\Delta x, \Delta z)$ at the $(n+1)$th frame, where Δx and Δz denote the instantaneous displacements in the lateral and axial directions, respectively, between two consecutive frames.

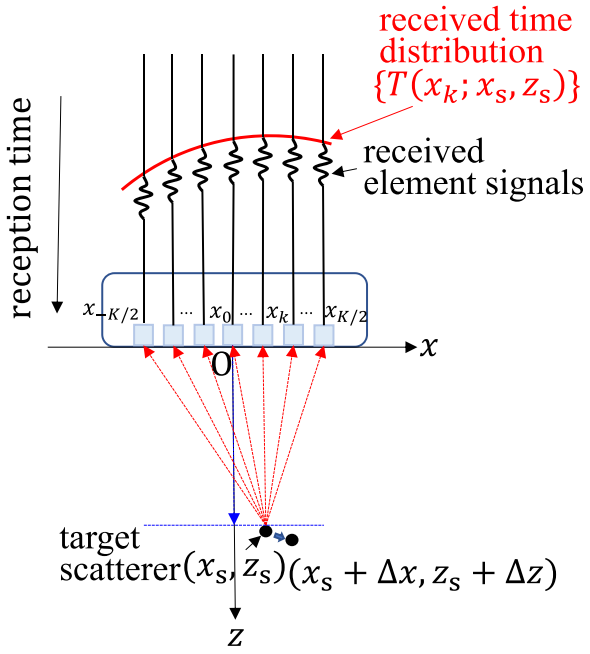

Fig. 1. (Color online) Time distribution $\{T(x_k; x_s, z_s)\}$ of scattered waves received by the probe elements after the plane wave is transmitted. The blue arrows show the propagation path of the plane wave from the probe to the target scatterer, and the red arrows show the propagation path from the target scatterer at the position (x_s, z_s) to each element at the nth frame. The target scatterer is displaced by $(\Delta x, \Delta z)$ at the $(n + 1)$th frame.

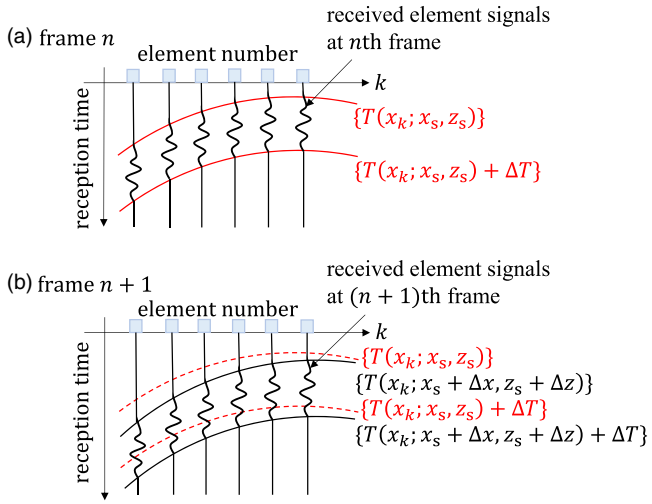

Fig. 2. (Color online) Principle of the proposed method to estimate 2D displacement $(\Delta x, \Delta z)$ of the target from nth frame to the $(n + 1)$th frame. (a) Time distribution $\{T(x_k; x_s, z_s)\}$ of RF signals of probe elements and the region with the length ΔT between the two red lines, where ΔT corresponds to the duration time of the scattered waves. (b) Time distribution $\{T(x_k; x_s + \Delta x, z_s + \Delta z)\}$ scattered from the target at $(x_s + \Delta x, z_s + \Delta z)$ at the $(n + 1)$th frame (black line).

Let the centre element position at $x_0 = 0$ among $(K + 1)$ elements be the origin. After the plane wave is transmitted from all elements of the probe at time 0, it is scattered by the target at positions (x_s, z_s), and then the RF signal is received by each element of the probe. The first arrival time $T(x_k; x_s, z_s)$ of the scattered wave received by the kth element at x_k is expressed as the round-trip propagation distance divided by the speed c_0 of sound in the medium as follows:

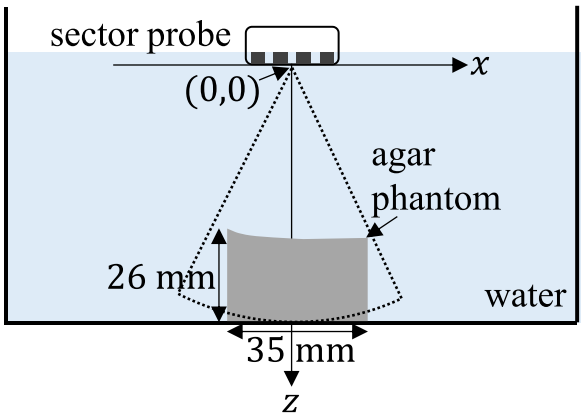

Fig. 3. (Color online) Schematic of the water tank experimental system with the agar phantom.

$$T(x_k; x_s, z_s) = \frac{z_s}{c_0} + \frac{\sqrt{z_s^2 + (x_s - x_k)^2}}{c_0}, \quad \left(\text{for } k = -\frac{K}{2}, \ldots, 0, \ldots, \frac{K}{2}\right) \tag{1}$$

where $(K + 1)$ is the number of probe elements.

Figure 2(a) illustrates the time distribution $\{T(x_k; x_s, z_s)\}$ of the RF signals on the probe elements. The region with length ΔT between the two red lines shows the duration time of the scattered waves from the target, where the region starts at the first arrival time $T(x_k; x_s, z_s)$. Figure 2(b) shows the $\{T(x_k; x_s + \Delta x, z_s + \Delta z)\}$ scattered from the target at $(x_s + \Delta x, z_s + \Delta z)$ at the $(n + 1)$th frame. Owing to the instantaneous 2D displacements $(\Delta x, \Delta z)$ of the measurement target, the time distribution of the scattered waves changed from red to black lines.

For a sufficiently high frame rate, the change in the waveforms of the waves scattered from the target between the two frames can be assumed to be small. Thus, the assumed instantaneous 2D displacements $(\Delta x, \Delta z)$ of the target between the frames can be evaluated by the following 2D complex cross-correlation $C_n(\Delta x, \Delta z; x_s, z_s)$ using the correlation window with length ΔT:

$$C_n(\Delta x, \Delta z; x_s, z_s) = \frac{1}{A} \sum_{k=-K/2}^{K/2} \sum_{t=0}^{\Delta T} y_{n,k}^*(T(x_k; x_s, z_s) + t) \cdot y_{n+1,k}(T(x_k; x_s + \Delta x, z_s + \Delta z) + t), \tag{2}$$

where $y_{n,k}(t)$ is the complex waveform obtained via the application of quadrature demodulation to the waveform acquired by the kth element in the nth frame, * denotes the complex conjugate, and A is the multiple of the root mean squares of RF signals in the correlation window at the nth and $(n + 1)$th frames expressed as

$$A = \sqrt{\sum_{k=-K/2}^{K/2} \sum_{t=0}^{\Delta T} |y_{n,k}(T(x_k; x_s, z_s) + t)|^2} \cdot \sqrt{\sum_{k=-K/2}^{K/2} \sum_{t=0}^{\Delta T} |y_{n+1,k}(T(x_k; x_s + \Delta x, z_s + \Delta z) + t)|^2}. \tag{3}$$

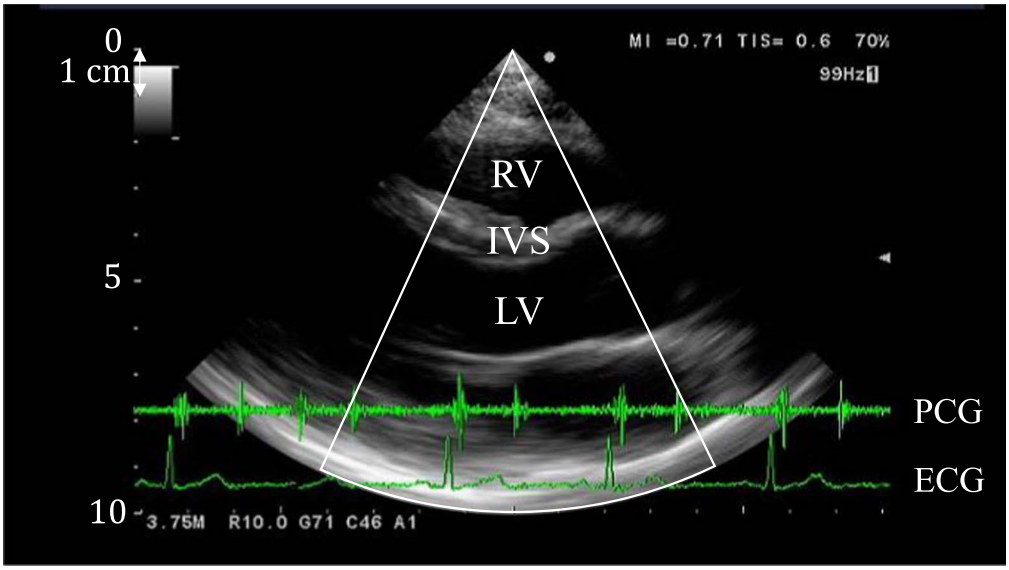

Fig. 4. (Color online) B-mode image of a parasternal left ventricular longitudinal view obtained by the ultrasound diagnosis apparatus for subject A. RV, IVS, LV, ECG, and PCG are the abbreviations of the right ventricle, the interventricular septum, the left ventricle, electrocardiogram, and phonocardiogram (heart sound), respectively.

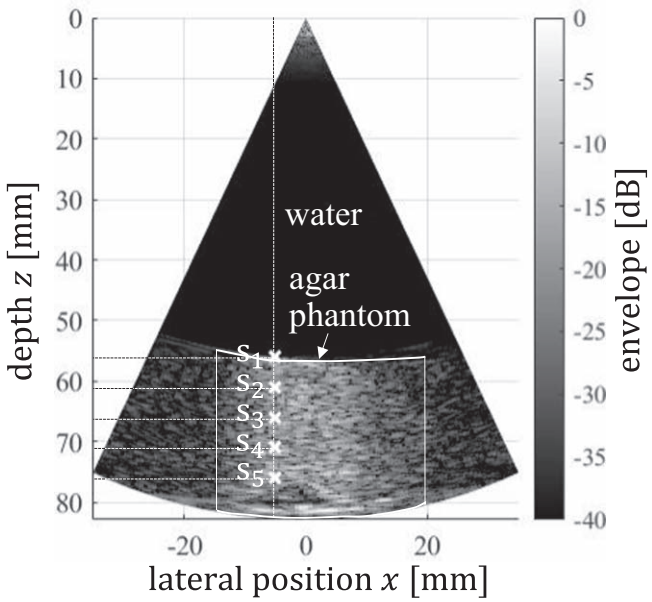

Fig. 5. B-mode image of the phantom in Fig. 3 with a width of the lateral view of 50° and the positions of five targets s_1, s_2, s_3, s_4, and s_5 set in the agar phantom.

The instantaneous 2D displacement of the target is determined by finding the assumed displacements $(\widehat{\Delta x},\ \widehat{\Delta z})$ that maximise the absolute value of $C_n(\Delta x,\ \Delta z;\ x_s,\ z_s)$ as

$$(\widehat{\Delta x},\ \widehat{\Delta z}) = \arg \max_{(\Delta x,\ \Delta z)\in\Re} |C_n(\Delta x,\ \Delta z;\ x_s,\ z_s)|, \qquad (4)$$

where $\Re$ denotes the range for search in axial and lateral directions.

When the non-target scatterer is set at $(x_{s_0},\ z_{s_0})$ at the nth frame, which is then displaced by $(\Delta x_{s_0},\ \Delta z_{s_0})$ at the $(n+1)$ th frame, the scattered waves from the target scatterer at positions $(x_s,\ z_s)$ and those from the non-target scatterer at positions $(x_{s_0},\ z_{s_0})$ are overlaid. However, the time difference distribution of the scattered waves from the target scatterer, $\{T(x_k;\ x_s+\Delta x,\ z_s+\Delta z)\} - \{T(x_k;\ x_s,\ z_s)\}$, differs from that of the scattered waves from the non-target scatterer, $\{T(x_k;\ x_{s_0}+\Delta x_{s_0},\ z_{s_0}+\Delta z_{s_0})\} - \{T(x_k;\ x_{s_0},\ z_{s_0})\}$. Thus, it is expected that the absolute values of $C_n(\Delta x,\ \Delta z;\ x_s,\ z_s)$ of Eq. (2) exhibits the highest value at the position corresponding to the 2D displacement $(\Delta x,\ \Delta z)$ for the target.

2.2. Phantom experiment

To verify the accuracy of the proposed method, it was used to measure 2D displacement of a phantom in a water tank experiment, where the phantom was created by mixing agar (concentration of approximately 10%) with water. Although the agar phantom did not include a scatterer, we confirmed that scattered waves from inside the agar phantom were received based on its inhomogeneity. The phantom with 26 and 35 mm in the axial and lateral directions, respectively as shown in Fig. 3, was measured. The phantom was set in a water tank, and the probe was moved in the x–z stage. The displacement of the probe was set as $\Delta z = -0.2$ mm in the axial direction and $\Delta x = 1$ mm in the lateral direction, which were determined based on the maximum instantaneous 2D displacement of the human myocardium at the IVS between the consecutive frames during the rapid filling phase at a frame rate of 200 Hz.

The element RF signals were acquired after the transmission of the single-plane wave using an ultrasound diagnostic apparatus (Prosound SSD-α10, Hitachi Aloka, Japan). The number of elements in the sector probe was $K = 95$, with an element spacing of 0.2 mm (UST-52101N, Aloka). The centre and sampling frequencies of the transmitted wave were 3.75 and 30 MHz, respectively. Since the water temperature was 26.7 °C, the speed of sound was calculated to be 1501 m s^{-1}.[31)]

To calculating the 2D complex cross-correlation $C_n(\Delta x,\ \Delta z;\ x_s,\ z_s)$, the length ΔT of the correlation window was set to 0.8 μs (1.2 mm). To determine $(\Delta x,\ \Delta z)$ in Eq. (4), the range $\Re$ of ±1.2 mm was searched in the axial and lateral directions.

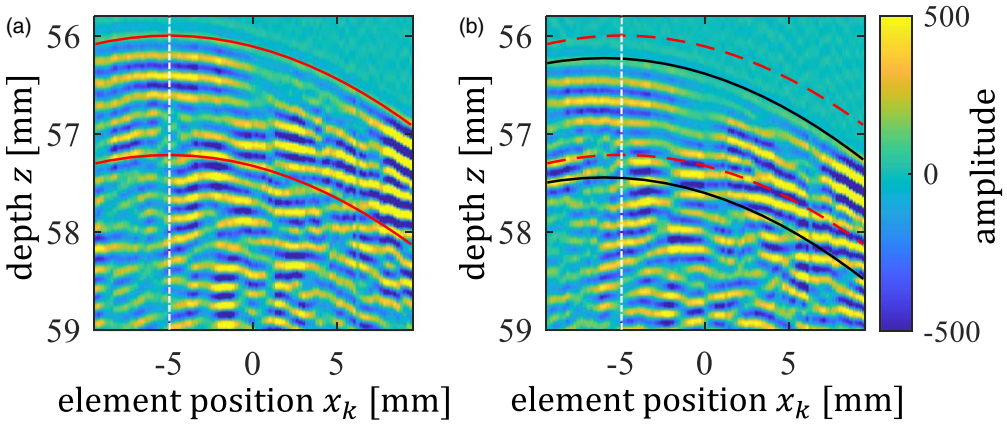

Fig. 6. (Color online) (a) Amplitudes of the element signals acquired before displacing the probe in Fig. 3. The upper red line shows the received time distribution of scattered waves, $\{T(x_k;\, x_{s_1},\, z_{s_1})\}$, for the target s_1 at $(x_{s_1},\, z_{s_1}) = (-5\text{ mm},\ 56\text{ mm})$. The lower red line shows the end time of the correlation window $\{T(x_k;\, x_{s_1},\, z_{s_1}) + \Delta T\}$. (b) Amplitudes of the element signals acquired after displacing the probe's position by $(\Delta x,\ \Delta z) = (1\text{ mm},\ -0.2\text{ mm})$. The red dashed lines: the distributions $\{T(x_k;\, x_{s_1},\, z_{s_1})\}$ and $\{T(x_k;\, x_{s_1},\, z_{s_1}) + \Delta T\}$ in Fig. 6(a). The black lines show the distributions $\{T(x_k;\, x_{s_1} + \widehat{\Delta x},\, z_{s_1} + \widehat{\Delta z})\}$ and $\{T(x_k;\, x_{s_1} + \widehat{\Delta x},\, z_{s_1} + \widehat{\Delta z}) + \Delta T\}$.

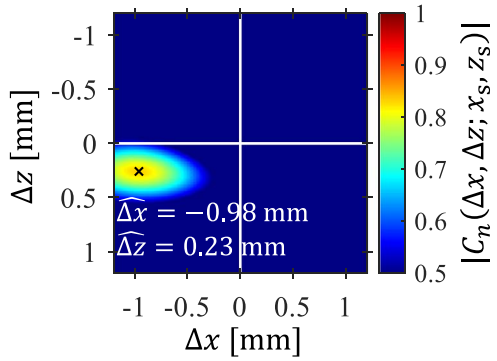

Fig. 7. (Color online) Magnitude distribution of the 2D complex cross-correlation, $|C_n(\Delta x,\ \Delta z;\, x_{s_1},\ z_{s_1})|$, obtained from element signals in Fig. 6(a) to those in Fig. 6(b).

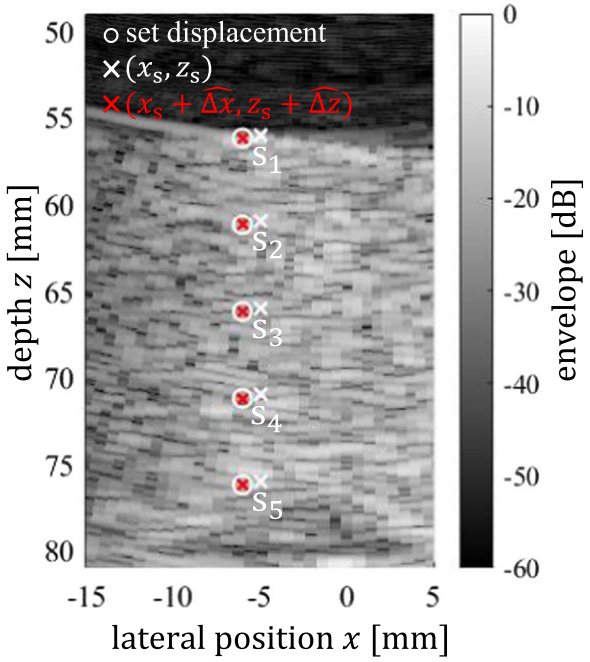

Fig. 8. (Color online) For each of the five targets s_1, s_2, s_3, s_4, and s_5, the position was set at the white cross mark before the displacement of the probe, as shown in Fig. 5. After the displacement of the probe, the true position of the 2D displacement (white circle) and the estimate (red cross mark) are shown for each target.

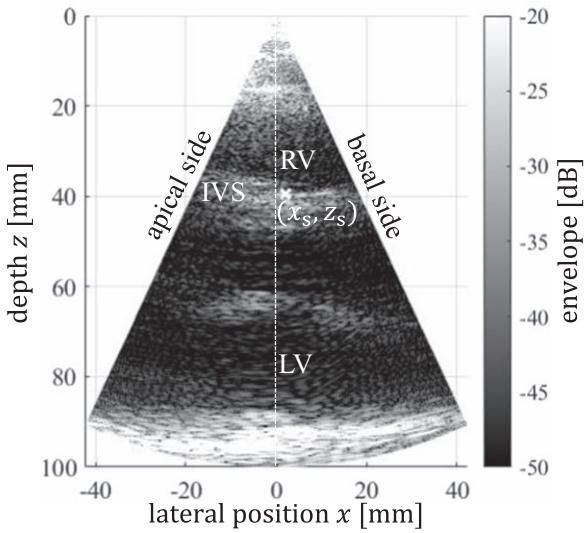

Fig. 9. For subject A, the B-mode image of a parasternal left ventricular longitudinal view with a width of the lateral view of 50° at the initial frame of the analysis (−100 ms from T_R for the first heartbeat). The position $(x_s,\ z_s) = (2.07\text{ mm},\ 39.57\text{ mm})$, where the 2D displacement of the IVS was measured, is shown by a white cross mark.

2.3. In vivo experiment

The proposed method was applied to the measurement of the 2D displacement of the IVS during one cardiac cycle and the results for each cardiac phase were discussed. The subjects were two healthy males in their 20s. Figure 4 shows a B-mode image of the parasternal left ventricular longitudinal view of subject A. The element RF signals from the IVS were acquired each time a plane wave was transmitted immediately below the probe. The speed of sound was set to 1540 m s^{-1}, and the frame rate was set to 1205 Hz, that is, the frame interval $\Delta T_s' = 830\ \mu$s. Although the theoretically achievable frame interval was $\Delta T_s = 166\ \mu$s for the employed ultrasound diagnosis equipment, $\Delta T_s' = 830\ \mu$s was set in the experiment owing to the transmission conditions for the equipment.

For calculating $C_n(\Delta x,\ \Delta z;\, x_s,\ z_s)$, the length ΔT of the correlation window was set to 0.78 μs(1.2 mm). Further, to

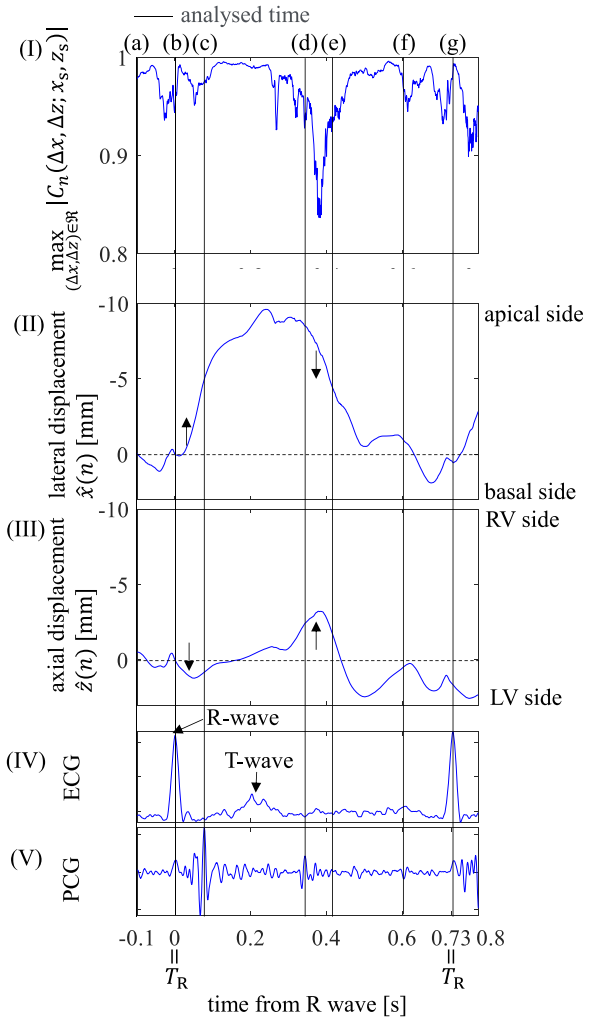

Fig. 10. (Color online) (I) Maximum absolute value of the 2D complex cross-correlation $|C_n(\Delta x,\ \Delta z;\ x_s,\ z_s)|$ for each frame n, (II) estimated $\hat{x}(n)$ of the lateral displacement, (III) estimated $\hat{z}(n)$ of the axial displacement, (IV) ECG, and (V) PCG, during one cardiac cycle for subject A. For the seven typical times (a)–(g), element RF signals and the distribution of the 2D complex cross-correlation are shown in Fig. 11.

determine $(\Delta x,\ \Delta z)$ in Eq. (4), a range $\Re$ of ±0.4 mm was set in the axial and lateral directions. These measurements were approved by the Ethics Committee of the Graduate School of Engineering, Tohoku University, and all the participants provided consent before participating in the present study.

3. Results and discussion

3.1. Phantom experiment

Figure 5 shows the B-mode image of the phantom in Fig. 3 with a lateral view width of 50°, and a solid closed line surrounding the phantom. Five measurement positions, s_1, s_2, s_3, s_4, and s_5 were set in the phantom, as shown in Fig. 5.

Figure 6(a) shows the amplitudes of the element signals acquired before displacing the probe (Fig. 3). For target s_1 at $(x_{s_1}, z_{s_1}) = (-5\text{ mm},\ 56\text{ mm})$, the received time distribution of scattered waves, $\{T(x_k; x_{s_1}, z_{s_1})\}$, was determined using Eq. (1), as indicated by the red upper line. The end time distribution of the correlation window, $\{T(x_k; x_{s_1}, z_{s_1}) + \Delta T\}$, is also indicated by the lower red line.

Because the phantom surface was not flat, as shown in Fig. 3, and the phantom was closest to the probe at $x_k = -5$ mm, the lateral measurement position x_{s_i} was set to −5 mm for all targets ($i = 1, \ldots, 5$). For targets s_2, s_3, s_4, and s_5, the axial positions $\{z_{s_i}\}$ were set apart by 5 mm in the range of 61– 76 mm in depth (Fig. 5).

Figure 6(b) shows the amplitudes of the element signals acquired after displacing the probe position by $(\Delta x,\ \Delta z) = (1\text{ mm},\ -0.2\text{ mm})$. The distributions $\{T(x_k; x_{s_1}, z_{s_1})\}$ and $\{T(x_k; x_{s_1}, z_{s_1}) + \Delta T\}$ in Fig. 6(a) are indicated by red dashed lines. For the assumed positions $(\widehat{\Delta x},\ \widehat{\Delta z})$, the distributions $\{T(x_k; x_{s_1} + \widehat{\Delta x}, z_{s_1} + \widehat{\Delta z})\}$ and $\{T(x_k; x_{s_1} + \widehat{\Delta x}, z_{s_1} + \widehat{\Delta z}) + \Delta T\}$ are represented by black lines, where $(\widehat{\Delta x},\ \widehat{\Delta z})$ are determined by the position with the maximum correlation value (Fig. 7). A comparison of Figs. 6(a) and 6(b) revealed that the received time distribution of the scattered waves shifted almost parallel from the positions of the red lines to those of the black lines according to the 2D displacement of $(\Delta x,\ \Delta z) = (1\text{ mm},\ -0.2\text{ mm})$.

Figure 7 shows the magnitude distribution of the 2D complex cross-correlation, $|C_n(\Delta x,\ \Delta z;\ x_s,\ z_s)|$, of Eq. (2), from the element RF signals in Fig. 6(a) to those in Fig. 6(b). From the position with the maximum correlation value of $|C_n(\Delta x,\ \Delta z;\ x_s,\ z_s)|$ in Fig. 7, the instantaneous 2D displacement of the target s_1 was estimated to be $(\widehat{\Delta x},\ \widehat{\Delta z}) = (-0.98\text{ mm},\ 0.23\text{ mm})$, which was consistent with the set displacement $(-\Delta x,\ -\Delta z) = (-1\text{ mm},\ +0.2\text{ mm})$ for the phantom as described above.

Figure 8 shows the 2D displacement estimate for each of the targets s_1, s_2, s_3, s_4, and s_5 in Fig. 5, which is indicated by the red cross mark. The white circle indicates the true position after the 2D displacement of each target. The mean and standard deviation of the 2D displacement of these five targets in Fig. 5 for the lateral and axial directions were $(\widehat{\Delta x},\ \widehat{\Delta z}) = (-1.004 \pm 0.023\text{ mm},\ 0.234 \pm 0.008\text{ mm})$. As shown in Fig. 8, the 2D displacement estimated for each target matched well with the set displacement $(-\Delta x,\ -\Delta z) = (-1\text{ mm},\ +0.2\text{ mm})$.

3.2. In vivo experiment

Figure 9 shows the B-mode image of a parasternal left ventricular longitudinal view for subject A with a lateral view width of 50° at the initial frame of the analysis (−100 ms from the time T_R of the R-wave for the first heartbeat). The target was set in the IVS at position $(x_s,\ z_s) = (2.07\text{ mm},\ 39.57\text{ mm})$, where its 2D displacement was measured below. The target was set by selecting the brightest position in the B-mode image.

Figure 10 shows the (I) maximum value of the $|C_n(\Delta x,\ \Delta z;\ x_s,\ z_s)|$ for each frame n, (II) estimated $\hat{x}(n)$ of the lateral displacement, (III) estimated $\hat{z}(n)$ of the axial displacement, (IV) electrocardiogram (ECG), and (V) phonocardiogram (PCG) during one cardiac cycle for subject A. As shown in Figs. 10(II) and 10(III), each displacement waveform was reset to 0 at T_R for the first heartbeat (time 0).

Seven typical times (a)–(g) were chosen (Fig. 10): (a) initial frame, (b) beginning of the isovolumetric contraction phase (T_R for the first heartbeat), (c) beginning of the ejection phase (the time of the first heart sound), (d) beginning of the isovolumetric relaxation phase (the time of the second heart sound), (e) the rapid filling phase, (f) beginning of the atrial systole (the time of P-wave for the second heartbeat), and (g) T_R for the second heartbeat.

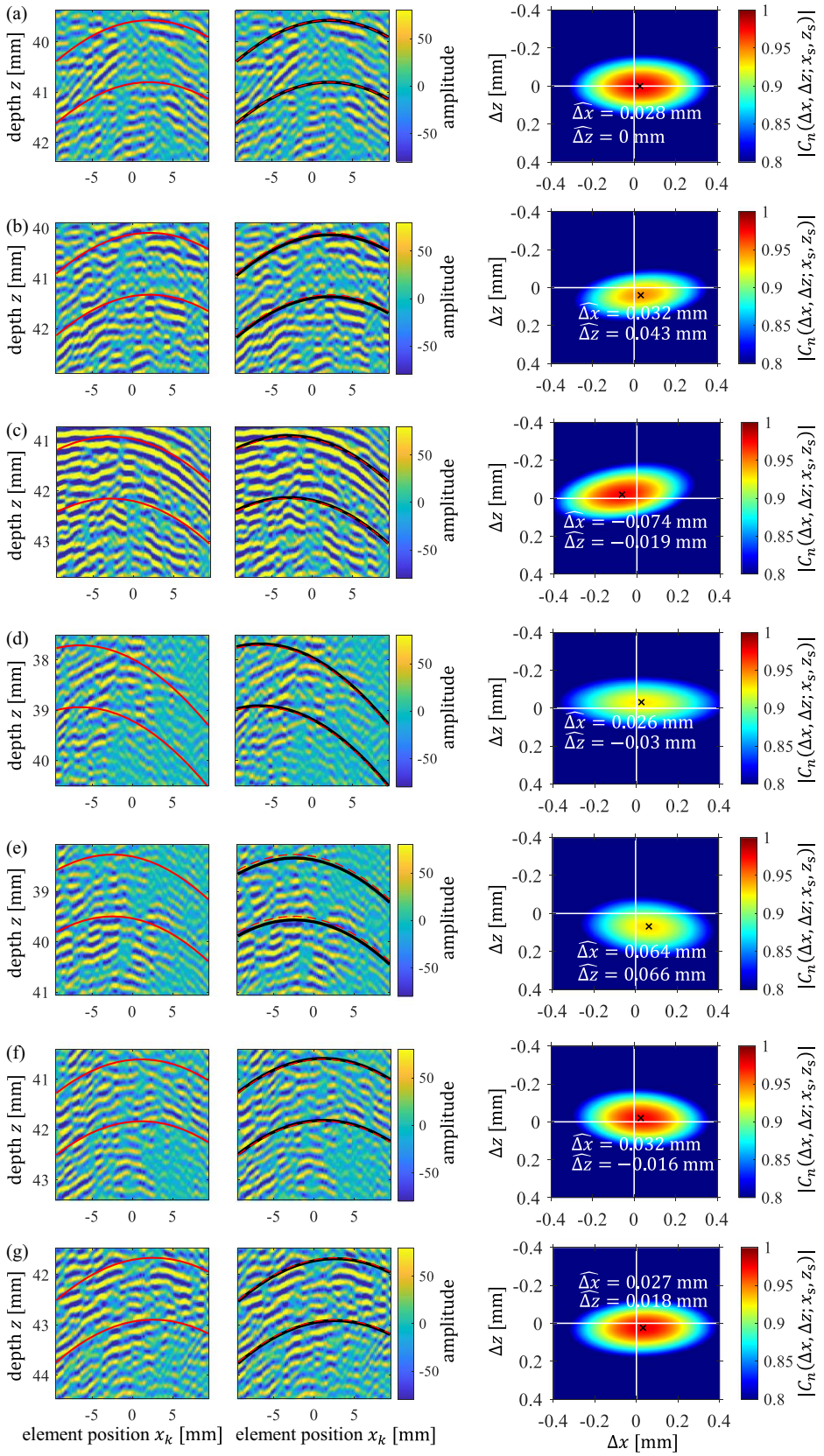

Fig. 11. (Color online) (left) Amplitudes of the element signals with $\{T(x_k; x_s, z_s)\}$ and $\{T(x_k; x_s, z_s) + \Delta T\}$ for two consecutive frames and (right) $|C_n(\Delta x,\ \Delta z;\ x_s,\ z_s)|$, at the seven typical times (a) to (g) for subject A. (a) Initial frame, (b) beginning of the isovolumetric contraction phase (T_R for the first heartbeat), (c) beginning of the ejection phase, (d) beginning of the isovolumetric relaxation phase, (e) the rapid filling phase, (f) beginning of the atrial systole, and (g) T_R for the second heartbeat.

As shown in Figs. 10(II) and 10(III), the heart wall rapidly moved toward the apical side and the left ventricle from (b) to (c), which corresponds to the movement of the myocardium during systole. Following the movement of the heart wall toward the basal side and the right ventricle from (d) to (f), it moved toward the left ventricle, which corresponded to the movement of the myocardium during diastole.

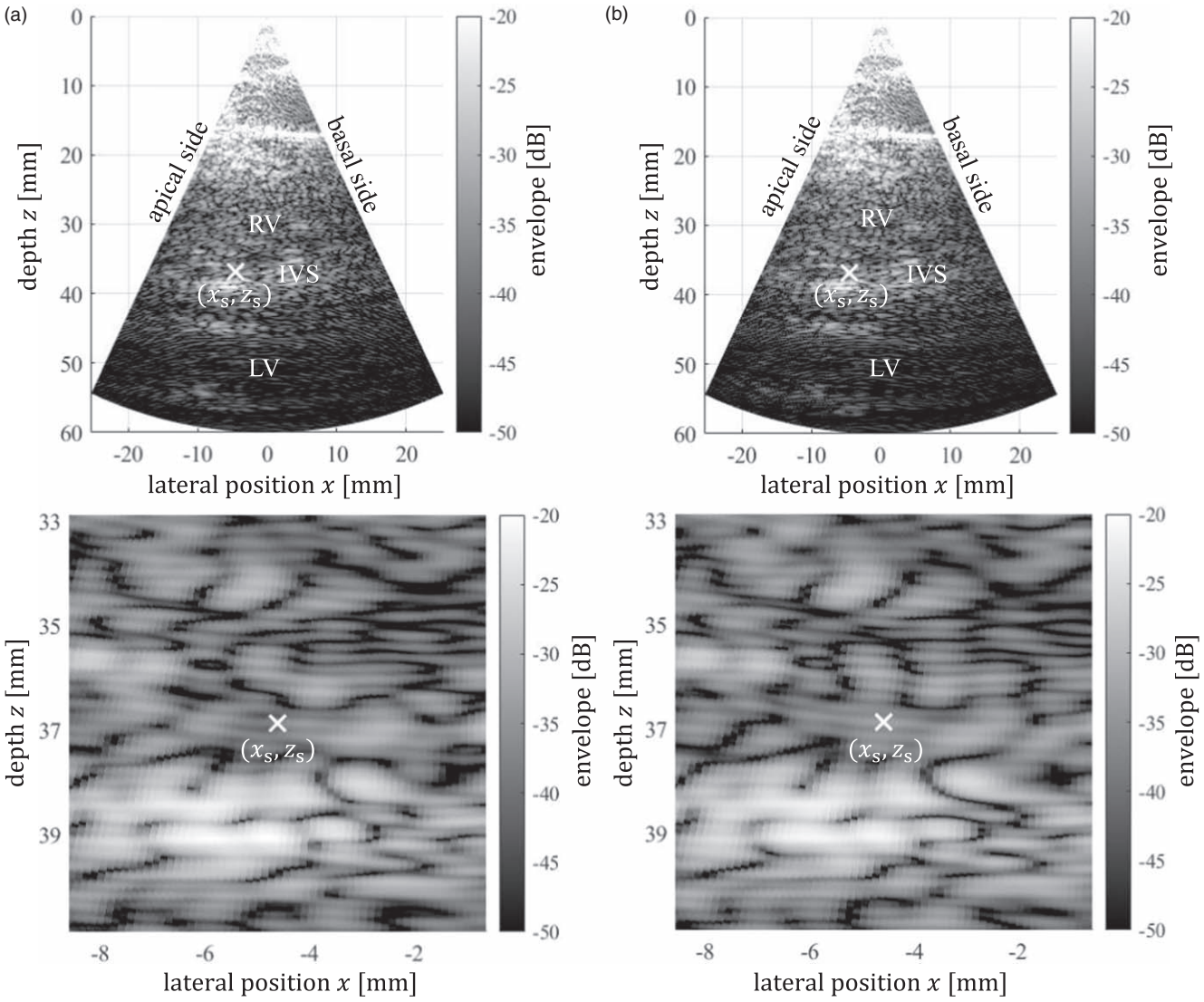

Fig. 12. (top) For subject A, the B-mode image of a parasternal left ventricular longitudinal view and (bottom) B-mode image magnified near the measurement position $(x_s,\ z_s)$. (a) One frame before when $\max_{(\Delta x,\ \Delta z)\in\Re} |C_n(\Delta x,\ \Delta z;\ x_s,\ z_s)|$ was lowest (381.8 ms from T_R for the first heartbeat), $(x_s,\ z_s) = (-4.66\ \text{mm},\ 36.87\ \text{mm})$. (b) Time when $\max_{(\Delta x,\ \Delta z)\in\Re} |C_n(\Delta x,\ \Delta z;\ x_s,\ z_s)|$ was lowest (382.63 ms from T_R for the first heartbeat), $(x_s,\ z_s) = (-4.61\ \text{mm},\ 36.87\ \text{mm})$.

Figure 11 shows the amplitudes of the element signals with $\{T(x_k;\ x_s,\ z_s)\}$ and $\{T(x_k;\ x_s,\ z_s) + \Delta T\}$ for two consecutive frames and $|C_n(\Delta x,\ \Delta z;\ x_s,\ z_s)|$ at seven times (a)–(g). From the initial frame to the beginning of the ejection phase, as shown in Figs. 11(a)–11(c), the correlation distribution was unimodal. However, from the isovolumetric relaxation phase to the rapid filling phase, as shown in Figs. 11(d) and 11(e), the amplitude of the element RF signals decreased, and the correlation distribution then became lower and obscured. For atrial systole, as shown in Figs. 11(f) and 11(g), both the amplitude of the element RF signal and the correlation increased again.

Figure 12(a) shows the B-mode image of a parasternal left ventricular longitudinal view for subject A at one frame before when $\max_{(\Delta x,\Delta z)\in\Re} |C_n(\Delta x,\ \Delta z;\ x_s,\ z_s)|$ was lowest (381.8 ms from T_R for the first heartbeat) during the rapid filling period between (d) and (e) in Fig. 10 and its magnified image around the measurement position $(x_s,\ z_s) = (-4.66\ \text{mm},\ 36.87\ \text{mm})$. Figure 12(b) shows the B-mode image of the same view when $\max_{(\Delta x,\ \Delta z)\in\Re} |C_n(\Delta x,\ \Delta z;\ x_s,\ z_s)|$ was lowest (382.63 ms from T_R for the first heartbeat) and its magnified image around the position $(x_s,\ z_s) = (-4.61\ \text{mm},\ 36.87\ \text{mm})$. These B-mode images were obtained by normalising the envelope amplitude of the received beams to the same value as in Fig. 9. Comparisons of the magnified images in Figs. 12(a) and 12(b) showed that the speckle pattern near the position $(x_s,\ z_s)$ in the IVS changed during $\Delta T_s' = 830\ \mu\text{s}$ between two consecutive frames, which would be caused by the rapid thinning of the heart wall. Thus, the decrease in the correlation distribution shown in Figs. 11(d) and 11(e) was caused by a change in waveforms owing to the change in thickness of the heart wall.

Figure 13 shows the maximum values of $|C_n(\Delta x,\ \Delta z;\ x_s,\ z_s)|$ for the same data set at the initial frame of Fig. 10(a) for various frame rates (the time interval from the initial frame). The maximum values significantly decreased for a frame rate of less than 100 Hz owing to the change in waveforms between frames with lower time resolution. However, for a high temporal resolution (=1205 Hz) as achieved in the proposed method, the correlation increased to estimate the instantaneous 2D displacement.

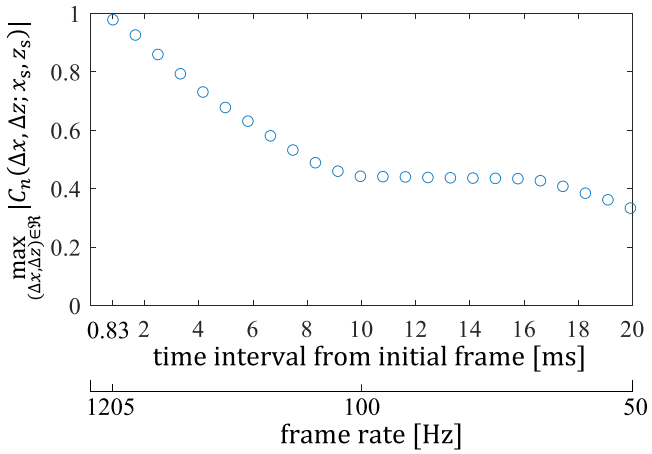

Fig. 13. (Color online) Maximum values of $|C_n(\Delta x,\ \Delta z;\ x_s,\ z_s)|$ for the same data set at the initial frame of Fig. 10(a) for various frame rates (the time interval from the initial frame).

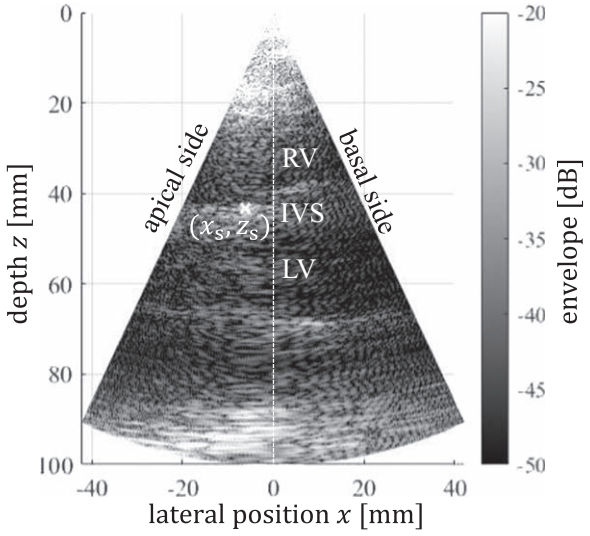

Fig. 14. For subject B, the B-mode image of a parasternal left ventricular longitudinal view at the initial frame of the analysis (−100 ms from T_R for the first heartbeat). The position $(x_s,\ z_s) = (-6.02\ \text{mm},\ 43.2\ \text{mm})$, where the 2D displacement of the IVS was measured, is shown by a white cross mark.

For subject B, Fig. 14 shows the B-mode image of a parasternal left ventricular longitudinal view at the initial frame of the analysis (−100 ms from T_R for the first heartbeat). The target was set in the IVS at position $(x_s,\ z_s) = (-6.02\ \text{mm},\ 43.2\ \text{mm})$, where the target was set by selecting the brightest in the B-mode image.

Figure 15 shows the (I) maximum value of the $|C_n(\Delta x,\ \Delta z;\ x_s,\ z_s)|$ for each frame n, (II) estimates $\hat{x}(n)$ of the lateral displacement, (III) estimates $\hat{z}(n)$ of the axial displacement, (IV) ECG, and (V) PCG, during one cardiac cycle for subject B. As shown in Figs. 15(II) and 15(III), the target moved toward the apical side and the left ventricle from (c) to (d) during the systole, and it moved toward the basal side and the right ventricle from (d) to (g) during the diastole, similar to subject A as shown in Figs. 10(II) and 10(III). Further, as shown in Figs. 10(II), 10(III), 15(II), and 15(III), the maximum displacements in the lateral direction and the axial direction for subjects A and B were $(\widehat{x_{\max}},\ \widehat{z_{\max}}) = (-9.64\ \text{mm},\ -3.2\ \text{mm})$ and

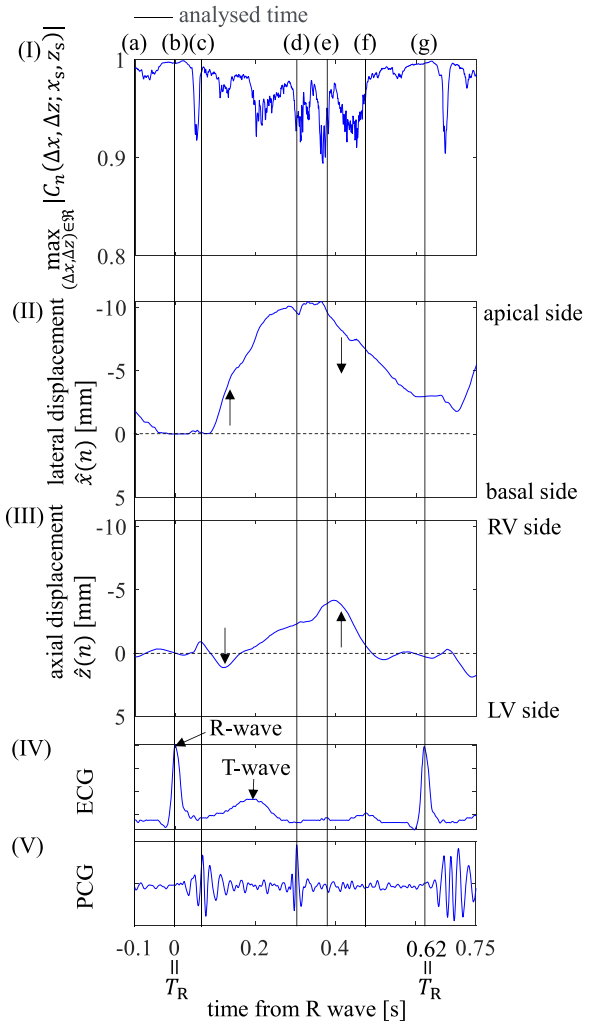

Fig. 15. (Color online) (I) Maximum absolute value of the 2D complex cross-correlation $|C_n(\Delta x,\ \Delta z;\ x_s,\ z_s)|$, (II) estimates $\hat{x}(n)$ of the lateral displacement, (III) estimates $\hat{z}(n)$ of the axial displacement, (IV) ECG, and (V)PCG, during one cardiac cycle for subject B. For the seven typical times (a)–(g), element RF signals and the distribution of the 2D complex cross-correlation are shown in Fig. 16.

$(-10.4\ \text{mm},\ -4.76\ \text{mm})$, respectively, which were in the same order as the previous study $(-8\ \text{mm},\ -3\ \text{mm})$.[32,33]

Figure 16 shows the amplitudes of the element signals with $\{T(x_k;\ x_s,\ z_s)\}$ and $\{T(x_k;\ x_s,\ z_s) + \Delta T\}$ for two consecutive frames and $|C_n(\Delta x,\ \Delta z;\ x_s,\ z_s)|$ at seven typical times (a) to (g), as shown in Fig. 15 for subject B. From the isovolumetric relaxation phase to the rapid filling phase, as shown in Figs. 16(d) and 16(e), the amplitude of the element RF signals decreased. Subsequently, the correlation distribution reduced and obscured, similar to that observed in subject A, as shown in Figs. 11(d) and 11(e). For the atrial systole, as shown in Figs. 16(f) and 16(g), both the amplitude of the element RF signal and the correlation increased again, similar to that observed in subject A, as shown in Figs. 11(f) and 11(g).

3.3. Comparison between the proposed and speckle tracking methods

To demonstrate the superiority of our method, we compared the proposed method with previous studies using the speckle tracking method and received time distribution. First, we compared the proposed method with a conventional speckle tracking method.

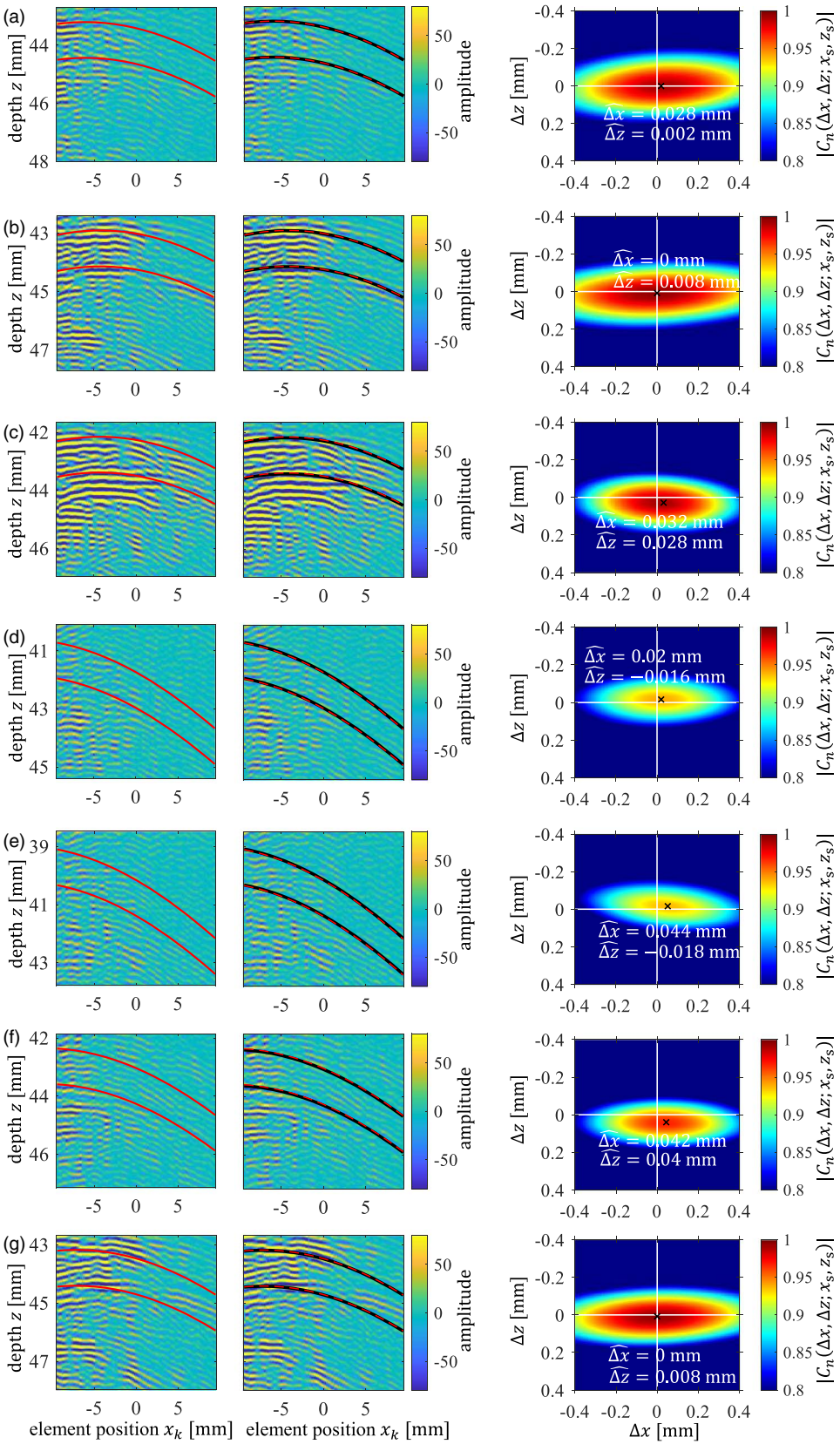

Fig. 16. (Color online) (left) Amplitudes of the element signals with $\{T(x_k; x_s, z_s)\}$ and $\{T(x_k; x_s, z_s) + \Delta T\}$ for two consecutive frames and (right) $|C_n(\Delta x, \Delta z; x_s, z_s)|$, at the seven typical times (a) to (g) for subject B. (a) Initial frame, (b) beginning of the isovolumetric contraction phase (the time T_R of the R-wave for the first heartbeat), (c) beginning of the ejection phase, (d) the beginning of the isovolumetric relaxation phase, (e) the rapid filling phase, (f) beginning of the atrial systole, and (g) T_R for the second heartbeat.

Figure 17 shows the (I) estimated $\widehat{\Delta x}(n)$ of the instantaneous lateral displacement, (II) estimated $\widehat{\Delta z}(n)$ of the instantaneous axial displacement, (III) ECG, and (IV) PCG, during one cardiac cycle for subject A.

For the conventional speckle tracking method, upon assuming 112 beams being employed to obtain the 2D envelope signals with a width of the lateral view of 42°, a period of $112 \times \Delta T_s = 18.59$ ms was necessary to acquire

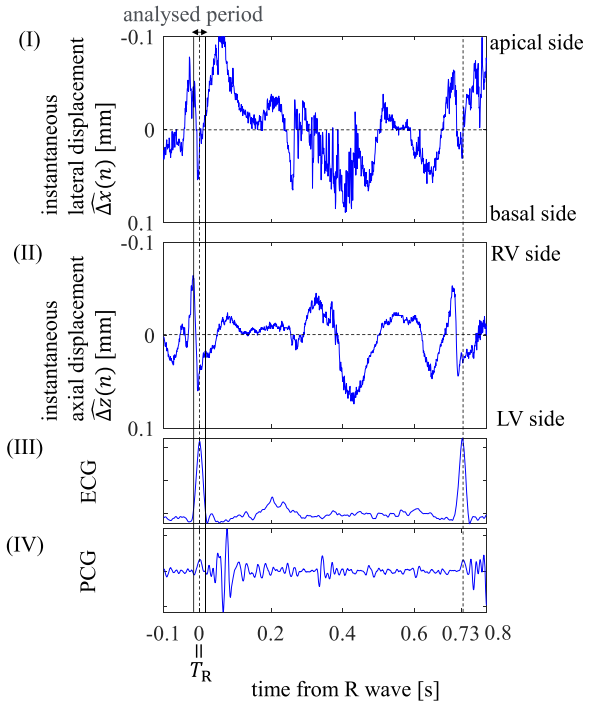

Fig. 17. (Color online) (I) Estimated $\widehat{\Delta x}(n)$ of the instantaneous lateral displacement, (II) estimated $\widehat{\Delta z}(n)$ of the instantaneous axial displacement, (III) ECG, and (IV) PCG, during one cardiac cycle for subject A.

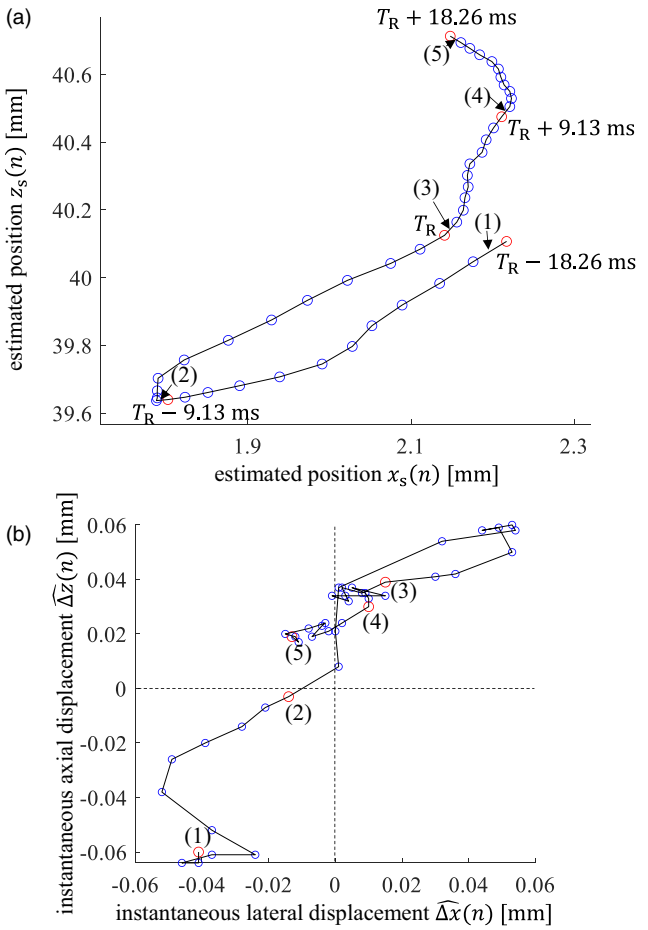

Fig. 18. (Color online) (a) Transition in the estimated positions $\{(x_s(n), z_s(n))\}$ of the target for 45 frames from $T_R - 18.26$ ms to $T_R + 18.26$ ms. The five typical times (1) to (5) were shown by the red circles, that is, (1) $T_R - 18.26$ ms, (2) $T_R - 9.13$ ms, (3) T_R, (4) $T_R + 9.13$ ms, and (5) $T_R + 18.26$ ms. (b) Transition in the estimated 2D instantaneous displacements $\{(\widehat{\Delta x}(n), \widehat{\Delta z}(n))\}$ in Fig. 17. The estimates at the five typical times were shown by the red circles.

the 2D signal when the transmitting interval $\Delta T_s = 166\,\mu$s. For two consecutive frames, twice of 18.59 ms, that is, 37.18 ms was necessary, which provides the time resolution of the conventional speckle tracking method and it was approximately 44 times longer than the frame interval employed in the present experiment, $\Delta T_s' = 830\,\mu$s.

Figure 18(a) shows the transition in the estimated positions $\{(x_s(n), z_s(n))\}$ of the target for 45 frames from $T_R - 18.26$ ms to $T_R + 18.26$ ms in Fig. 17. The five typical times (1)–(5) are shown by the red circles, that is, (1) $T_R - 18.26$ ms, (2) $T_R - 9.13$ ms, (3) T_R, (4) $T_R + 9.13$ ms, and (5) $T_R + 18.26$ ms.

For this period, the transition in the estimated 2D instantaneous displacements $\{(\widehat{\Delta x}(n), \widehat{\Delta z}(n))\}$ in Fig. 17 is shown in Fig. 18(b), and the estimates at the five typical times are shown by red circles. As shown in Fig. 18(b), the 2D instantaneous displacement rapidly changed in short intervals of $44 \times \Delta T_s' = 36.52$ ms. Therefore, the instantaneous change in the 2D displacement in Fig. 18 cannot be measured using the conventional speckle tracking method.

However, a previous study had already attempted to measure the 2D displacement of the heart wall using parallel receive beamforming to improve the temporal resolution to 1020 Hz,[15] which shows that the superiority of the proposed method cannot be obtained with respect to time resolution. A theoretical comparison of the performance of this method and the proposed method is the subject of future work.

3.4. Comparison of the proposed method with those of previous studies using received time distribution

Next, we compared our method with previous studies[28,29] using the received time distribution of scattered waves on the elements in the ultrasonic probe. The time difference distribution $\Delta T(x_k; x_s, z_s, \Delta x, \Delta z)$ between $T(x_k; x_s, z_s)$ of Eq. (1) and $T(x_k; x_s + \Delta x, z_s + \Delta z)$ is expressed as

$$\begin{aligned}\Delta T(x_k; x_s, z_s, \Delta x, \Delta z) &= T(x_k; x_s + \Delta x, z_s + \Delta z) - T(x_k; x_s, z_s) \\ &= \frac{\Delta z}{c_0} + \frac{\sqrt{(z_s + \Delta z)^2 + (x_s + \Delta x - x_k)^2}}{c_0} - \frac{\sqrt{z_s^2 + (x_s - x_k)^2}}{c_0}. \end{aligned} \tag{5}$$

Using the following three assumptions

$$z_s^2 \gg (x_k - x_s)^2, \tag{6}$$

$$|\Delta x| \ll |x_{K/2}|, \tag{7}$$

$$|\Delta z| \ll z_s, \tag{8}$$

the time difference distribution $\Delta T(x_k; x_s, z_s, \Delta x, \Delta z)$ in Eq. (5) can be approximated by the following linear function regarding the element position x_k as

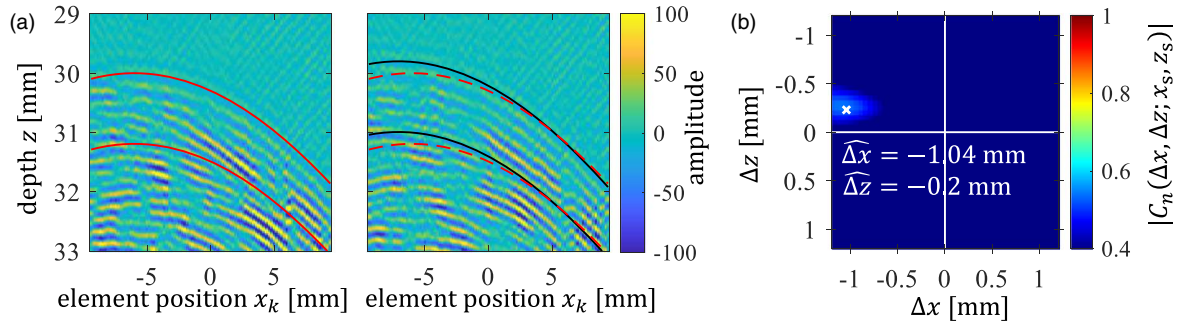

Fig. 19. (Color online) (a) Amplitudes of the element signals with $\{T(x_k;\, x_s,\, z_s)\}$ and $\{T(x_k;\, x_s,\, z_s) + \Delta T\}$ acquired before and after displacing the position of the probe by $(\Delta x,\ \Delta z) = (1\text{ mm},\ 0.2\text{ mm})$, respectively. (b) Magnitude distribution of the 2D complex cross-correlation $|C_n(\Delta x,\ \Delta z;\, x_s,\ z_s)|$.

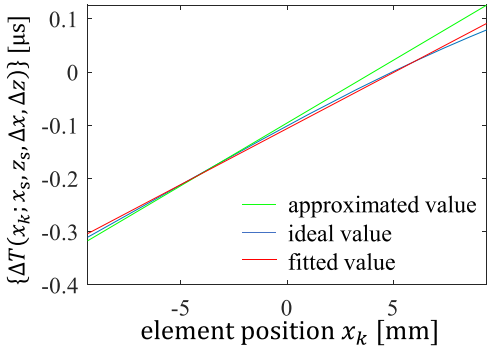

Fig. 20. (Color online) Time difference distribution $\Delta T(x_k;\, x_s,\ z_s,\ \Delta x,\ \Delta z)$ for $(\Delta x,\ \Delta z) = (-1\text{ mm},\ -0.2\text{ mm})$. The blue line shows the true value obtained in Eq. (5), the green line shows the approximated value in Eq. (9), and the red line shows the result by linearly fitting Eq. (9) to the actual data of the blue line.

$$\Delta T(x_k;\, x_s,\ z_s,\ \Delta x,\ \Delta z) \approx \frac{1}{c_0}\left\{\left(-\frac{x_s+\Delta x}{z_s+\Delta z}+\frac{x_s}{z_s}\right)x_k+\frac{1}{2}\frac{(x_s+\Delta x)^2}{z_s+\Delta z}-\frac{x_s^2}{2z_s}+2\Delta z\right\}. \quad (9)$$

In a previous study,[28] the measured time difference distribution $\Delta T(x_k;\, x_s,\ z_s,\ \Delta x,\ \Delta z)$ was linearly fitted using the least-squares method, and the 2D displacement $(\widehat{\Delta x_p},\ \widehat{\Delta z_p})$ was estimated from the slope and intercept of Eq. (9).

We compared the 2D displacements of the agar phantom estimated by the proposed method and this previous study in a water tank experiment of Fig. 3 as follows. The phantom was set in a water tank, and the probe was moved in the x–z stage. The displacement of the probe was set as $\Delta z = 0.2$ mm and $\Delta x = 1$ mm in the axial and lateral directions, respectively. The target was set in the phantom at position $(x_s,\ z_s) = (-7\text{ mm},\ 30\text{ mm})$, assuming that the lateral position of the target x_s moved away from the centre of the probe.

Figure 19(a) shows the amplitudes of the element signals acquired before and after displacing the probe by $(\Delta x,\ \Delta z) = (1\text{ mm},\ 0.2\text{ mm})$, respectively. The time distributions $\{T(x_k;\, x_s,\, z_s)\}$ and $\{T(x_k;\, x_s,\, z_s) + \Delta T\}$ are indicated by the red lines in Fig. 19(a). For the assumed position $(\widehat{\Delta x},\ \widehat{\Delta z})$, the distributions $\{T(x_k;\, x_s + \widehat{\Delta x},\, z_s + \widehat{\Delta z})\}$ and $\{T(x_k;\, x_s + \widehat{\Delta x},\, z_s + \widehat{\Delta z}) + \Delta T\}$ are indicated by the black lines in Fig. 19(a). Figure 19(b) shows $|C_n(\Delta x,\ \Delta z;\, x_s,\ z_s)|$ and the 2D displacement was estimated to be $(\widehat{\Delta x},\ \widehat{\Delta z}) = (-1.04\text{ mm},\ -0.2\text{ mm})$, which was consistent with the true value $(-\Delta x,\ -\Delta z) = (-1\text{ mm},\ -0.2\text{ mm})$.

Figure 20 shows the time difference distribution $\Delta T(x_k;\, x_s,\ z_s,\ \Delta x,\ \Delta z)$ for $(\Delta x,\ \Delta z) = (-1\text{ mm},\ -0.2\text{ mm})$. The blue line represents the true value obtained using Eq. (5), the green line represents the approximated value in Eq. (9), and the red line shows the result obtained by linearly fitting Eq. (9) to the actual data of the blue line. From the slope and intercept of the red line, the 2D displacement estimated by the method of a previous study[28] was obtained as $(\widehat{\Delta x_p},\ \widehat{\Delta z_p}) = (-0.9\text{ mm},\ -0.14\text{ mm})$. Compared to the previous study, the 2D displacement estimated by the proposed method was closer to the set value, as shown in Fig. 19.

In another previous study,[29] after obtaining $\{\Delta T(x_k;\, x_s,\ z_s,\ \Delta x,\ \Delta z)\}$, two elements were selected, and the 2D displacement was estimated from the simultaneous equations of the round-trip propagation paths. This method yielded a lower signal-to-noise ratio than using all elements; therefore, 2D displacement estimation is expected to be less accurate. Based on these comparisons, it can be concluded that the proposed method can estimate the 2D displacement more accurately than previous studies.[28,29]

4. Conclusions

This paper proposed a novel 2D displacement estimation method with a high temporal resolution using a 2D complex cross-correlation comprising the element RF signals between frames based on the received time distribution of scattered waves from the target. A phantom experiment was conducted to examine the accuracy of the method, and the human heart experiment verified its usefulness in the evaluation of cardiac function.

In the phantom experiment, the estimated 2D displacement of the phantom was consistent with the set displacement, confirming that the proposed method can estimate the 2D displacement of the phantom. In the in vivo experiment, we measured the 2D displacement of the IVS during one cardiac cycle. However, during the rapid filling phase, the maximum value of the cross-correlation decreased because of the change in the RF waveforms. However, there are certain aspects to be considered. The effect of changes in each element of the RF signal scattered from the myocardium caused by contraction and dilation on the correlation should be considered to further improve the accuracy. Moreover, in this study, the length (ΔT) and width $(K + 1)$ of the correlation window were fixed. Thus, to improve the accuracy, these parameters should be considered. Furthermore, the limitations, that is, the lower and higher limits, in estimating the instantaneous 2D displacement by the proposed method should be considered.

Acknowledgments

This work was supported in part by JSPS KAKENHI 21H03835.

1) W. N. McDicken, G. R. Sutherland, C. M. Moran, and L. N. Gordon, Ultrasound Med. Biol. **18**, 651 (1992).
2) H. Kanai, H. Hasegawa, N. Chubachi, Y. Koiwa, and M. Tanaka, IEEE Trans. Ultrason. Ferroelectr. Freq. Control **44**, 752 (1997).
3) A. Heimdal, A. Støylen, H. Torp, and T. Skjærpe, J. Am. Soc. Echocardiogr. **11**, 1013 (1998).
4) G. R. Sutherland, G. Di Salvo, P. Claus, J. D'hooge, and B. Bijnens, J. Am. Soc. Echocardiogr. **17**, 788 (2004).
5) J. Grondin, V. Sayseng, and E. E. Konofagou, IEEE Trans. Ultrason. Ferroelectr. Freq. Control **64**, 1212 (2017).
6) Y. Obara, S. Mori, M. Arakawa, and H. Kanai, Jpn. J. Appl. Phys. **60**, SDDE02 (2021).
7) P. Liu, J.-W. Muller, H.-M. Schwab, and R. Lopata, Front. Phys. **10**, 1 (2022).
8) D. Durrer, R. Th. Van Dam, G. E. Freud, M. J. Janse, F. L. Meijler, and R. C. Arzbaecher, Circulation **41**, 899 (1970).
9) H. Kanai, IEEE Trans. Ultrason. Ferroelectr. Freq. Control **52**, 1931 (2005).
10) A. Hayashi, S. Mori, M. Arakawa, and H. Kanai, Jpn. J. Appl. Phys. **58**, SGGE05 (2019).
11) A. Basarab, P. Gueth, H. Liebgott, and P. Delachartre, IEEE Trans. Ultrason. Ferroelectr. Freq. Control **56**, 945 (2009).
12) Y. Honjo, H. Hasegawa, and H. Kanai, Jpn. J. Appl. Phys. **49**, 07HF14 (2010).
13) D. Asari, H. Hasegawa, and H. Kanai, Jpn. J. Appl. Phys. **53**, 07KF21 (2014).
14) M. V. Andersen, C. Moore, K. Arges, P. Søgaard, L. R. Østergaard, S. E. Schmidt, J. Kisslo, and O. T. Von Ramm, Ultrasond Med. Biol. **42**, 2606 (2016).
15) P. Joos, J. Porée, H. Liebgott, D. Vray, M. Baudet, J. Faurie, F. Tournoux, G. Cloutier, B. Nicolas, and D. Garcia, IEEE Trans. Ultrason. Ferroelectr. Freq. Control **65**, 720 (2018).
16) M. Mozumi, R. Nagaoka, and H. Hasegawa, Jpn. J. Appl. Phys. **58**, SGGE02 (2019).
17) M. Orlowska, A. Ramalli, A. Petrescu, M. Cvijic, S. Bézy, P. Santos, J. Pedrosa, J.-U. Voigt, and J. D'hooge, IEEE Trans. Ultrason. Ferroelectr. Freq. Control **67**, 1764 (2020).
18) H. Chen, T. Varghese, P. S. Rahko, and J. A. Zagzebski, Ultrasonics **49**, 98 (2009).
19) V. Mor-Avi et al., J. Am. Soc. Echocardiogr. **24**, 277 (2011).
20) J.-U. Voigt et al., Eur. Heart. J. Cardiovasc. Imaging **16**, 1 (2015).
21) D. P. Shattuck, M. D. Weinshenker, S. W. Smith, and O. T. von Ramm, J. Acoust. Soc. Am. **75**, 1273 (1984).
22) S. Langeland, J. D'hooge, H. Torp, B. Bijnens, and P. Suetens, Ultrasound Med. Biol. **29**, 1177 (2003).
23) H. Hasegawa and H. Kanai, J. Med. Ultrason. **38**, 129 (2011).
24) C. Papadacci, M. Pernot, M. Couade, M. Fink, and M. Tanter, IEEE Trans. Ultrason. Ferroelectr. Freq. Control **61**, 288 (2014).
25) R. Nagaoka, M. Mozumi, and H. Hasegawa, Jpn. J. Appl. Phys. **58**, SGGE10 (2019).
26) N. Furusawa, S. Mori, M. Arakawa, and H. Kanai, Jpn. J. Appl. Phys. **58**, SGGA08 (2019).
27) K. Sugahara, S. Mori, M. Arakawa, and H. Kanai, Jpn. J. Appl. Phys. **60**, SDDE05 (2021).
28) S.-L. Wang, M.-L. Li, and P.-C. Li, IEEE Trans. Ultrason. Ferroelectr. Freq. Control **54**, 70 (2007).
29) P. Kruizinga, F. Mastik, J. G. Bosch, N. de Jong, A. F. W. van der Steen, and G. van Soest, IEEE Trans. Ultrason. Ferroelectr. Freq. Control **62**, 1733 (2015).
30) K. Hara, S. Mori, M. Arakawa, and H. Kanai, Proc. Symp. Ultrason. Electr. **43**, 3Pa5-11 (2022).
31) W. Kroebel and K.-H. Mahrt, Acta Acustica United Acustica **35**, 154 (1976).
32) C. Ma and T. Varghese, Ultrasonics **53**, 782 (2013).
33) T. Asai, H. Taki, and H. Kanai, IEEJ Trans. Electron. Inf. Syst. **137**, 573 (2017).

